Compensated Semimetal LaSb with Unsaturated Magnetoresistance

L.-K. Zeng,[1] R. Lou,[2] D.-S. Wu,[1] Q. N. Xu,[1] P.-J. Guo,[2] L.-Y. Kong,[1] Y.-G. Zhong,[1] J.-Z. Ma,[1] B.-B. Fu,[1]
P. Richard,[1,3] P. Wang,[1] G. T. Liu,[1] L. Lu,[1,3] Y.-B. Huang,[4] C. Fang,[1] S.-S. Sun,[2] Q. Wang,[2] L. Wang,[1]
Y.-G. Shi,[1] H. M. Weng,[1,3] H.-C. Lei,[2] K. Liu,[2] S.-C. Wang,[2,*] T. Qian,[1,3,†] J.-L. Luo,[1,3,‡] and H. Ding[1,3]

[1]*Beijing National Laboratory for Condensed Matter Physics, and Institute of Physics,
Chinese Academy of Sciences, Beijing 100190, China*
[2]*Department of Physics and Beijing Key Laboratory of Opto-electronic Functional Materials & Micro-nano Devices,
Renmin University of China, Beijing 100872, China*
[3]*Collaborative Innovation Center of Quantum Matter, Beijing, China*
[4]*Shanghai Synchrotron Radiation Facility, Shanghai Institute of Applied Physics,
Chinese Academy of Sciences, Shanghai 201204, China*

By combining angle-resolved photoemission spectroscopy and quantum oscillation measurements, we performed a comprehensive investigation on the electronic structure of LaSb, which exhibits near-quadratic extremely large magnetoresistance (XMR) without any sign of saturation at magnetic fields as high as 40 T. We clearly resolve one spherical and one intersecting-ellipsoidal hole Fermi surfaces (FSs) at the Brillouin zone (BZ) center Γ and one ellipsoidal electron FS at the BZ boundary X. The hole and electron carriers calculated from the enclosed FS volumes are perfectly compensated, and the carrier compensation is unaffected by temperature. We further reveal that LaSb is topologically trivial but shares many similarities with the Weyl semimetal TaAs family in the bulk electronic structure. Based on these results, we have examined the mechanisms that have been proposed so far to explain the near-quadratic XMR in semimetals.

Magnetoresistance (MR) is the magnetic-field induced changes of electrical resistance of a material, which has attracted great attention not only in understanding the underlying physical mechanisms but also for practical applications, such as spintronics devices, magnetic memory, and magnetic field sensors. Negative MR has been discovered in many magnetic materials, such as giant MR in magnetic multilayer films [1,2] and colossal MR in perovskite manganites [3,4]. Extremely large positive MR (XMR) has been reported in nonmagnetic materials [5–10].

Recently, the discovery of XMR without any sign of saturation at magnetic fields up to 60 T in nonmagnetic semimetal WTe$_2$ has renewed research interest in this topic [11]. The magnetotransport in WTe$_2$ is characterized by a typical near-quadratic field dependence of MR and a field-induced up-turn in resistivity followed by a plateau at low temperature. Soon after, these fingerprints were also observed in several semimetals including TmPn$_2$ (Tm = Ta/Nb, Pn = As/Sb) [12–17], LnX (Ln = La/Y, X = Sb/Bi) [18–22], and ZrSiS [23–25]. These common features imply that the quadratic XMR in these nonmagnetic semimetals may have the same origin. XMR has also been observed in Dirac and Weyl semimetals like Cd$_3$As$_2$ [26,27], TaAs [28], and NbP [29], which, nevertheless, show a linear field dependence of MR distinct from the near-quadratic behavior. So far, several mechanisms have been proposed to explain the exotic quadratic XMR behavior, including electron-hole resonance compensation [11,30], forbidden backscattering at zero field [31], field-induced Fermi surface (FS) changes [12], and nontrivial band topology [18].

It is widely believed that XMR in semimetals is intimately related to their underlying electronic structures. First-principles calculations have shown that most of their electronic structures are rather complicated [10–15,32]. The experimental electronic structures by angle-resolved photoemission spectroscopy (ARPES) measurements are even more complicated and illegible because of the convoluted bulk and surface states [31,33–38]. The lack of unambiguous experimental data on the intrinsic electronic structures seriously obstructs the investigation on the underlying mechanism of quadratic XMR.

In this Letter, we report a comprehensive study on the electronic structure of LaSb by combining ARPES and quantum oscillation (QO) measurements. The FS topology of LaSb is clearly resolved, which consists of two hole FS pockets at the Brillouin zone (BZ) center Γ and one electron FS pocket at the BZ boundary X. We have precisely quantified the hole and electron carrier densities and demonstrated that LaSb is a compensated semimetal. The measured band structure confirms that LaSb is topologically trivial but with a linearly dispersive bulk band. As compared to other XMR semimetals, LaSb has a much simpler electronic structure, which facilitates the investigation on the origin of quadratic XMR.

High-quality single crystals of LaSb were grown by the flux method. ARPES measurements were performed at the Dreamline beam line of the Shanghai Synchrotron Radiation Facility (SSRF) with a Scienta D80 analyzer and at the beam line 13U of the National Synchrotron Radiation Laboratory (NSRL) at Hefei with a Scienta R4000

analyzer. The energy and angular resolutions were set to 15 meV and 0.05°, respectively. The samples were cleaved *in situ* along the (001) plane and measured at $T = 30$ and 200 K in a working vacuum better than 5×10^{-11} Torr.

Figure 1(a) shows the schematic of the crystal structure of LaSb. It has a simple rock salt structure, which is face-center cubic with space group $Fm\text{-}3m$. A typical cuboid single crystal of LaSb is shown in the inset of Fig. 1(b). X-ray diffraction (XRD) measurements on single crystals confirm that the rectangular face is the (001) plane. The electric current (I) and the magnetic field (H) in our magnetotransport measurements are applied along the (100) and (001)
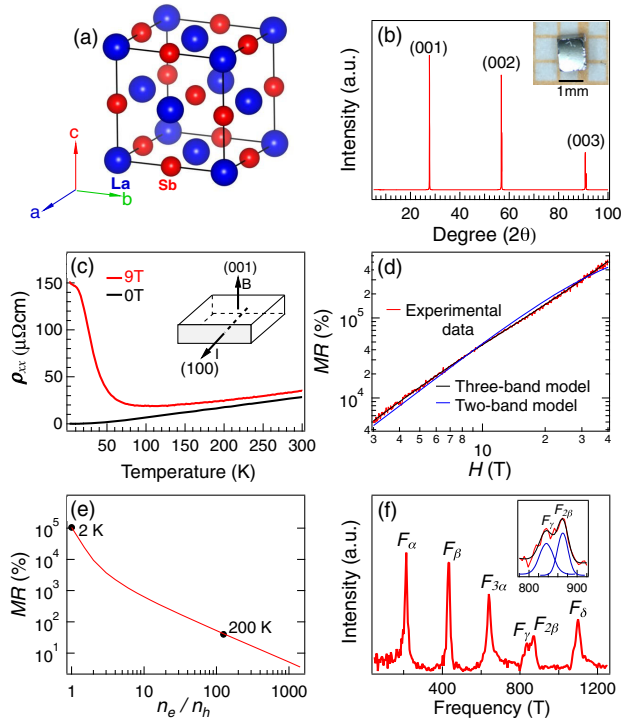

FIG. 1. Crystal structure and magnetotransport of LaSb. (a) Schematic crystal structure of LaSb. (b) XRD pattern on the (001) surface of single crystal. The inset shows a typical cuboid single crystal. (c) Resistivity as a function of temperature at magnetic field $H = 0$ (black curve) and 9 T (red curve). The inset illustrates the directions of H and I in the magnetotransport measurements. (d) $MR(\%) = [R(H)\text{-}R(0)]/R(0) \times 100\%$ plotted as a function of field up to 40 T at $T = 2$ K (red curve), where $R(H)$ and $R(0)$ represent the resistivity at magnetic field H and at zero field, respectively. Blue curve is the fitting to the two-band model considering slightly imperfect carrier compensation ($n_e/n_h = 0.998$). Black curve is the fitting to the three-band model with perfect carrier compensation. (e) Simulated MR as a function of the ratio n_e/n_h based on the two-band model. Solid circles represent the experimental MR at $T = 2$ and 200 K under 9 T assuming that the suppression of MR at high temperatures is attributed to carrier imbalance. (f) FFT spectrum of the Shubnikov–de Haas oscillations shown in the Supplemental Material [39]. The inset shows that the peak positions of F_γ and $F_{2\beta}$ are extracted by the fitting to two Gaussian functions.

directions, respectively, as illustrated in the inset of Fig. 1(c). In Fig. 1(c), the resistivity at zero field shows a metallic behavior in the measured temperature range from 2 to 300 K. When a magnetic field of 9 T is applied, the resistivity shows a minimum at a field-induced "turn on" temperature $T \sim 100$ K, and then increases dramatically with decreasing temperature. A resistivity plateau is ultimately formed after an inflection at $T \sim 15$ K, which is consistent with previous results on LaSb [18].

In Fig. 1(d), the MR curve as a function of magnetic field exhibits not any sign of saturation even up to 40 T. Unsaturated MR at magnetic fields up to several tens of Tesla has also been reported in other XMR semimetals like WTe$_2$ [11], LaBi [20], and ZrSiS [25]. The MR curve can be approximately fit to a power-law function with an exponent $m = 1.78$. Similar power-law field dependence with m slightly less than two has been observed in WTe$_2$ [40], PtSn$_4$ [10], NbSb$_2$ [12], and LaBi [19]. So far, the most commonly used mechanism to explain the quadratic XMR is the two-band model, which predicts a quadratic field dependence of MR as electron-hole compensation is satisfied [41]. The deviation from the quadratic behavior was simply attributed to slight imbalance between electrons and holes. We fit the data based on the two-band model considering imperfect carrier compensation [19,42] and obtain the ratio of electron-to-hole carrier density $n_e/n_h = 0.998$ by assuming equal electron and hole mobilities. Although the deviation from perfect compensation is negligible, the fitting curve exhibits an obvious trend of saturation, which does not reproduce the MR data. The two-band model is not sufficient to explain the near-quadratic behavior in LaSb and unlikely the deviation from quadratic in other XMR materials either. To understand the XMR in LaSb, we investigate comprehensively its electronic structure.

We demonstrate that the electron and hole carriers in LaSb are perfectly compensated by combining QO and ARPES measurements. The fast Fourier transform (FFT) spectrum of the QO data in Fig. 1(f) exhibits four principal frequencies: $F_\alpha = 214$ T with its third harmonic $F_{3\alpha} = 644$ T, $F_\beta = 436$ T with its second harmonic $F_{2\beta} = 875$ T, $F_\gamma = 836$ T, and $F_\delta = 1090$ T. Using the Onsager relation [$F = (\hbar/2\pi e)A_k$ between frequency F and the extreme cross section A_k of a FS], we extract the corresponding A_k values.

We further determine the topology of these FSs by ARPES measurements. Figures 2(b) and 2(c) show the intensity maps at the Fermi level (E_F) recorded at $T = 30$ K with photon energy $h\nu = 53$ and 83 eV, close to the $k_z = 0$ and π planes, respectively (See more photon energy dependence data in the Supplemental Material [39]). To examine temperature effects on the electronic structure, we also performed ARPES measurements with $h\nu = 53$ eV at $T = 200$ K and plot the FS intensity map in Fig. 2(d). The FS topology at $k_z = 0$ [Fig. 2(b)] is the same as at $k_z = \pi$ [Fig. 2(c)], but shifted by the wave vector (π, π), which is
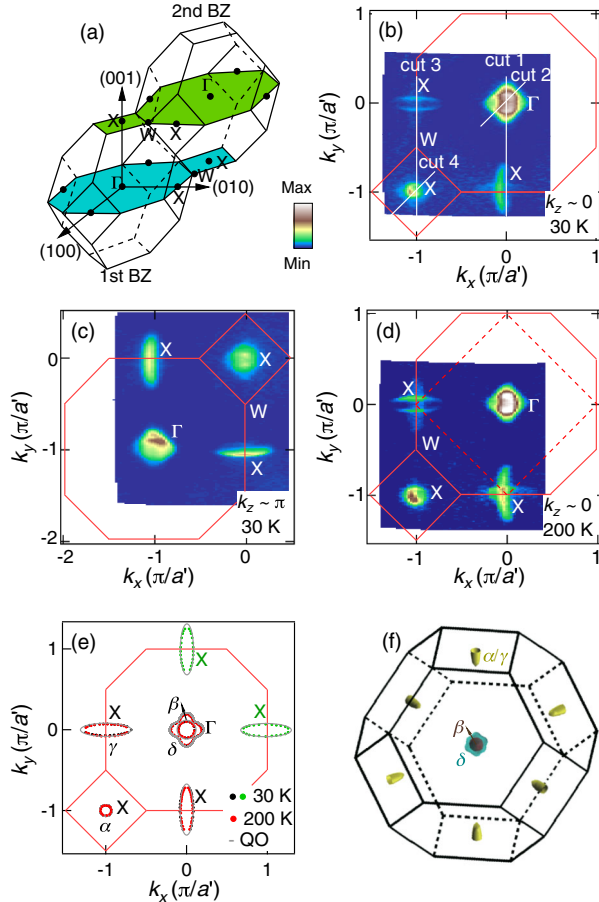
FIG. 2. Experimental and calculated FSs of LaSb. (a) Schematic of the first and second 3D BZs. The cyan and green areas illustrate the locations of the mapping data in (b) and (c), respectively. (b),(c) FS intensity plots obtained by integrating the photoemission intensity within $E_F \pm 10$ meV recorded with $h\nu = 53$ and 83 eV, close to the $k_z = 0$ and π planes, respectively, at $T = 30$ K. a' is the half of lattice constant $a(= 6.5$ Å) of the face-center-cubic unit cell. Cuts 1–4 in (b) indicate the momentum locations of the measured bands in Fig. 3. (d) Same as (b), but measured at $T = 200$ K. Dashed lines represent the (001) surface BZ. (e) Fermi wave vectors extracted from the data recorded with $h\nu = 53$ (black dots) and 83 eV (green dots) at $T = 30$ K and $h\nu = 53$ eV at $T = 200$ K (red dots). Solid lines are FSs derived from QOs. (f) Calculated 3D FSs with the MBJ potential.

illustrated in the schematic three-dimensional (3D) BZ in Fig. 2(a). We extract the Fermi wave vectors of the FSs and plot them as symbols in Fig. 2(e). The FSs at $k_z = 0$ in the first BZ consist of one circular and one intersecting-elliptical hole pockets at the BZ center Γ, and one elliptical electron pocket at the BZ boundary X with its long-axis along Γ-X. In addition, there is one small circular electron pocket at $X(-\pi, -\pi)$ in the second BZ. The experimental FS topology is consistent with the theoretical calculations in Fig. 2(f). Moreover, we observe some additional FSs around the X points in Figs. 2(b) and 2(d), which could be associated with the lattice periodic potential of the termination layer on

the (001) surface. As the ARPES experimental technique with vacuum ultraviolet lights is surface sensitive, the excited photoelectrons suffer from the influence of periodic potential on the (001) surface. As the consequence of broken translational symmetry along the (001) direction, the projected (001) surface BZ, illustrated as dashed lines in Fig. 2(d), is reduced by $1/\sqrt{2}$ as compared with the translation periodicity in the $k_x - k_y$ plane of bulk BZ. As a result, the band folding with a wave vector $Q = (\pi, \pi, 0)$, leads to the additional FSs around X. By comparing the FS areas in ARPES with the A_k values in QO, we assign the electron FSs at $X(-\pi, -\pi)$ and $(-\pi, 0)$ as α and γ, respectively, and the inner and outer hole FSs at Γ as β and δ, respectively, as indicated in Fig. 2(e). With the knowledge of the FS profiles, we derive the FSs from the A_k values and plot them as solid curves in Fig. 2(e), which are well consistent with those determined by ARPES.

As LaSb has a cubic crystal structure, its electronic structure is identical along the three directions k_x, k_y, and k_z of the BZ. The 3D structure of the FSs can thus be reconstructed by the regular 2D FSs in the $k_z = 0$ and π planes. The 3D FSs consist of one spherical and one intersecting-ellipsoidal hole FSs at Γ reconstructed by the β and δ FSs, respectively, and one ellipsoidal electron FS at X reconstructed by the α and γ FSs, which is elongated along $\Gamma - X$, as seen in Fig. 2(f). The regular 3D structure of these FSs enables us to precisely quantify the volume of each FS. Note that while the ARPES measurements do not map the FSs exactly at $k_z = 0$ and π, the extreme cross sections of the FSs at $k_z = 0$ and π can be accurately extracted from the QO data. Therefore, we calculate the volumes of the 3D FSs that are reconstructed with the 2D FSs derived from the QO data. The enclosed volumes of the β, δ, and α/γ FSs are 0.006 39, 0.0196, and 0.008 56 Å^{-3}, corresponding to carrier densities of 5.15×10^{19}, 1.58×10^{20}, and 6.90×10^{19} cm^{-3}, respectively. Considering that there are three electron α/γ FSs in one BZ, the ratio of electron-to-hole carrier density $n_e/n_h = 0.99$, indicating LaSb a compensated semimetal within the experimental accuracy. This is in conflict with the claim in Ref. [18], in which it is argued that LaSb is not compensated, but our result is in agreement with the previous reports [43,44]. Furthermore, the extracted FSs from the ARPES data measured at $T = 30$ and 200 K are exactly the same, as shown in Fig. 2(e), indicating that the condition of carrier compensation is held in a broad temperature range.

Figure 3 shows the near-E_F band dispersions along the high-symmetry lines recorded with $h\nu = 53$ eV, whose momentum locations are indicated in Fig. 2(b). We first discuss the topological nature of LaSb based on the band dispersions. First-principles electronic structure calculations show controversial results about the band topology, depending on the density functions used in the calculations [18,42,45]. In the calculation with the Perdew-Burke-Ernzerhof (PBE) function at the generalized gradient
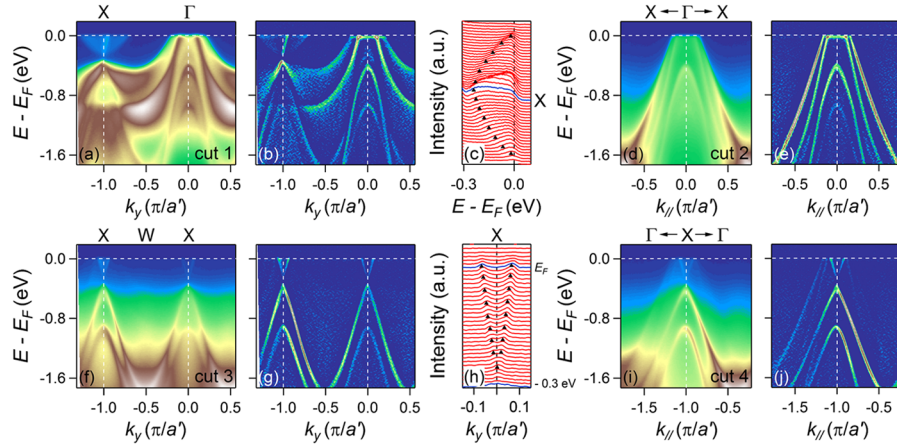
FIG. 3.   Near-E_F band dispersions along high-symmetry lines measured at $k_z \sim 0$ plane ($hv = 53$ eV). (a),(b) Photoemission intensity plot along $\Gamma - X$ [cut 1 in Fig. 2(b)] and corresponding 2D curvature intensity plot [48], respectively. (c) Energy distribution curves of (a) around X. (d),(e) Same as (a),(b) but rotated by 45° [cut 2 in Fig. 2(b)]. (f),(g) Same as (a),(b) but along $X - W - X$ [cut 3 in Fig. 2(b)]. (h) Momentum distribution curves of (f) around the right X. (i),(j) Same direction as in (d),(e) but around $X(-\pi, -\pi)$ [cut 4 in Fig. 2(b)]. The black dots in (c) and (h) indicate the peak positions, which track the dispersions of the electron band along and perpendicular to the long axis of the ellipsoidal γ FS, respectively. The linear electron band at X in (a)–(c) and the hole bands around X in (i) and (j) are a result of the band folding with a wave vector $Q = (\pi, \pi, 0)$.

approximation (GGA) level, the band inversion happens at X between the La d states and the Sb p states, suggesting that LaSb is a 3D topological insulator, whereas the calculation with the modified Becke-Johnson (MBJ) potential [46,47] at the meta-GGA level shows no band inversion at X [18,42]. The major discrepancy between the band structures in these two types of calculations is that there exists an anticrossing of two bands along $\Gamma - X$ in the former. To elucidate the band topology of LaSb, we analyze the experimental band dispersions along $\Gamma - X$. As shown in Figs. 3(a) and 3(b), on moving from Γ to X, the outer hole band gradually levels off and then curves upward, forming a hole band with a top at ~ -0.35 eV at X. In addition, there is a parabolic electron band along $\Gamma - X$ with a bottom at ~ -0.25 eV at X, forming a band gap of ~ 0.1 eV. Note that the linear electron band at X in Figs. 3(a)–3(c), which is associated with the additional FSs in Fig. 2(b), is a result of the band folding with a wave vector $Q = (\pi, \pi, 0)$. It is clear that there is no band anticrossing along $\Gamma - X$, which is at odds with the calculation with the PBE functional. In contrast, the experimental band dispersions are well reproduced by the calculations with the MBJ potential. We therefore conclude that LaSb is a topologically trivial material.

As our results confirm that LaSb is topologically trivial, no Dirac-like surface states are observed. Therefore, the 2D angle dependence of QOs reported previously [18] could not be a result of 2D surface state FSs associated with a topologically nontrivial phase. In contrast, the 2D transport behavior should arise from the ellipsoidal α/γ FS, which is largely elongated along $\Gamma - X$ with the ratio of long-axis to short-axis ~ 4. We further reveal that the highly anisotropic electron band associated with the α/γ FS disperses

parabolically along the long-axis [Figs. 3(a)–3(c)] but linearly along the short axis [Figs. 3(f)–3(j)]. Many materials exhibiting ultrahigh mobility possess linearly dispersive bands, such as Bi [49], Cd_3As_2 [27], TaAs [28], and NbP [29]. It is widely believed that the high mobility in these materials is associated with the linear bands. The linearly dispersive electron band may be the origin of the high mobility in LaSb.

We examine the proposed mechanisms for the XMR by comparing the electronic structure of LaSb with those of other XMR semimetals. First, in WTe_2 the measured FSs show dramatic changes with varying temperature [33,34], which spoils the carrier compensation. This was considered as the origin of the drastically suppressed XMR with increasing temperature. The suppression of MR is also observed in LaSb; for instance, the MR at 200 K is suppressed by 3 orders as compared to that at 2 K under 9 T. If the suppression is attributed to carrier imbalance, the ratio n_e/n_h has to be ~ 100 in the simulation based on the two-band model, as plotted in Fig. 1(e). This is contradictory to our ARPES results, which reveal no observable changes of the FSs with temperature in LaSb. Second, due to the lack of inversion symmetry in WTe_2, the spin degeneracy is removed by spin-orbit coupling, leading to a complicated spin texture of the bands, which has been claimed to play an important role in the XMR of WTe_2 [31]. This explanation is not applicable to LaSb because the inversion symmetry in LaSb preserves that its spins are doubly degenerate at zero field. Third, the field-induced insulator-like resistivity with a plateau is considered as the consequences of breaking time reversal symmetry in topological semimetals [18], whereas our results have demonstrated that LaSb is a topologically trivial material,

which excludes the possibility that the XMR is associated with nontrivial band topology. Fourth, it is worth noting that the bulk electronic structure of LaSb shares a considerable degree of similarity to that of the Weyl semimetal TaAs family, which consists of hole FSs from the normal parabolic bands and electron FSs from the linear Weyl bands [29,50]. These Weyl semimetals exhibit a linear MR [28,29] distinct from the near-quadratic behavior in LaSb, suggesting they should be associated with different origins.

While LaSb satisfies the two prerequisites for XMR in the two-band model, i.e., carrier compensation and ultrahigh mobility, the deviation from the quadratic behavior cannot be explained by a slightly imperfect carrier compensation. Thus we consider a three-band model within the general multiple-band picture [30]. Our ARPES results exhibit that the electron band is highly anisotropic along and perpendicular to the long-axis of the ellipsoidal FS while the two hole bands have similar dispersions near E_F. Based on the electronic structure, considering the magnetic field applied along the (001) direction, one can construct a three-band model including two kinds of electrons and one kind of hole. As seen in Fig. 1(d), the formula derived from the three-band model with carrier compensation [30] fits to the MR curve excellently. Further investigation is desirable to clarify if the near-quadratic XMR can be understood in the frame of the multiple-band picture. As a common behavior in many materials, the XMR remains puzzling by the complication from the band structures. LaSb with a simple electronic structure represents an ideal system to formulate a theoretical understanding to this exotic phenomenon.

*scw@ruc.edu.cn
†tqian@iphy.ac.cn
‡jlluo@iphy.ac.cn

[1] M. N. Baibich, J. M. Broto, A. Fert, F. Nguyen Van Dau, F. Petroff, P. Etienne, G. Creuzet, A. Friederich, and J. Chazelas, Phys. Rev. Lett. **61**, 2472 (1988).

[2] G. Binasch, P. Grunberg, F. Saurenbach, and W. Zinn, Phys. Rev. B **39**, 4828 (1989).

[3] *Colossal Magnetoresistive Oxides*, edited by Y. Tokura (Gordon and Breach, Amsterdam, 2000).

[4] *Colossal Magnetoresistive Manganites*, edited by T. Chatterji (Kluwer Academic, Dordrecht, 2004).

[5] L. Schubnikow and W. J. De Haas, Nature (London) **126**, 500 (1930).

[6] P. B. Alers and R. T. Webber, Phys. Rev. **84**, 863 (1951).

[7] T. Kasuya, M. Sera, and T. Suzuki, J. Phys. Soc. Jpn. **62**, 2561 (1993).

[8] F. Y. Yang, K. Liu, K. Hong, D. H. Reich, P. C. Searson, and C. L. Chein, Science **284**, 1335 (1999).

[9] R. Xu, A. Husmann, T. F. Rosenbaum, M.-L. Saboungi, J. E. Enderby, and P. B. Littlewood, Nature (London) **390**, 57 (1997).

[10] E. Mun, H. Ko, G. J. Miller, G. D. Samolyuk, S. L. Budko, and P. C. Canfield, Phys. Rev. B **85**, 035135 (2012).

[11] M. N. Ali, J. Xiong, S. Flynn, J. Tao, Q. D. Gibson, L. M. Schoop, T. Liang, N. Haldolaarachchige, M. Hirschberger, N. P. Ong, and R. J. Cava, Nature (London) **514**, 205 (2014).

[12] K. Wang, D. Graf, L. Li, L. Wang, and C. Petrovic, Sci. Rep. **4**, 7328 (2014).

[13] B. Shen, X. Y. Deng, G. Kotliar, and N. Ni, Phys. Rev. B **93**, 195119 (2016).

[14] D. S. Wu, J. Liao, W. Yi, X. Wang, P. G. Li, H. M. Weng, Y. G. Shi, Y. Q. Li, J. L. Luo, X. Dai, and Z. Fang, Appl. Phys. Lett. **108**, 042105 (2016).

[15] C. C. Xu, J. Chen, G. X. Zhi, Y. K. Li, J. H. Dai, and C. Cao, Phys. Rev. B **93**, 195106 (2016).

[16] Y.-Y. Wang, Q.-H. Yu, P.-J. Guo, K. Liu, and T.-L. Xia, Phys. Rev. B **94**, 041103 (2016).

[17] Z. Wang, Y. Li, Y. Lu, Z. Shen, F. Sheng, C. Feng, Y. Zheng, and Z. A. Xu, arXiv:1603.01717.

[18] F. F. Tafti, Q. D. Gibson, S. K. Kushwaha, N. Haldolaarachchige, and R. J. Cava, Nat. Phys. **12**, 272 (2015).

[19] S. S. Sun, Q. Wang, P. J. Guo, K. Liu, and H. C. Lei, New J. Phys. **18**, 082002 (2016).

[20] N. Kumar, C. Shekhar, S.-C. Wu, I. Leermakers, U. Zeitler, B. H. Yan, and C. Felser, Phys. Rev. B **93**, 241106 (2016).

[21] Q. Yu, Y. Wang, S. Xu, and T.-L. Xia, arXiv:1604.05912.

[22] O. Pavlosiuk, P. Swatek, and P. Wiśniewski, arXiv:1604.06945.

[23] R. Singha, A. Pariari, B. Satpati, and P. Mandal, arXiv:1602.01993.

[24] M. N. Ali, L. M. Schoop, C. Garg, J. M. Lippmann, E. Lara, B. Lotsch, and S. Parkin, arXiv:1603.09318.

[25] X. F. Wang, X. C. Pan, M. Gao, J. H. Yu, J. Jiang, J. R. Zhang, H. K. Zuo, M. H. Zhang, Z. X. Wei, W. Niu, Z. C. Xia, X. G. Wan, Y. L. Chen, F. Q. Song, Y. B. Xu, B. G. Wang, G. H. Wang, and R. Zhang, Adv. Electron. Mater. **2**, 1600228 (2016).

[26] J. Feng, Y. Pang, D. Wu, Z. Wang, H. Weng, J. Li, X. Dai, Z. Fang, Y. Shi, and L. Lu, Phys. Rev. B **92**, 081306 (2015).

[27] T. Liang, Q. Gibson, M. N. Ali, M. Liu, R. J. Cava, and N. P. Ong, Nat. Mater. **14**, 280 (2015).

[28] X. C. Huang, L. X. Zhao, Y. J. Long, P. P. Wang, D. Chen, Z. H. Yang, H. Liang, M. Q. Xue, H. M. Weng, Z. Fang, X. Dai, and G. F. Chen, Phys. Rev. X **5**, 031023 (2015).

[29] C. Shekhar, A. K. Nayak, Y. Sun, M. Schmidt, M. Nicklas, I. Leermakers, U. Zeitler, Z. K. Liu, Y. L. Chen, W. Schnelle, J. Grin, C. Felser, and B. H. Yan, Nat. Phys. **11,** 645 (2015).

[30] T. Kasuya, M. Sera, Y. Okayama, and Y. Haga, J. Phys. Soc. Jpn. **65,** 160 (1996).

[31] J. Jiang, F. Tang, X. C. Pan, H. M. Liu, X. H. Niu, Y. X. Wang, D. F. Xu, H. F. Yang, B. P. Xie, F. Q. Song, P. Dudin, T. K. Kim, M. Hoesch, P. K. Das, I. Vobornik, X. G. Wan, and D. L. Feng, Phys. Rev. Lett. **115,** 166601 (2015).

[32] Q. N. Xu, Z. D. Song, S. M. Nie, H. M. Weng, Z. Fang, and X. Dai, Phys. Rev. B **92,** 205310 (2015).

[33] I. Pletikosić, M. N. Ali, A. V. Fedorov, R. J. Cava, and T. Valla, Phys. Rev. Lett. **113,** 216601 (2014).

[34] Y. Wu, N. H. Jo, M. Ochi, L. Huang, D. Mou, S. L. Bud'ko, P. C. Canfield, N. Trivedi, R. Arita, and A. Kaminski, Phys. Rev. Lett. **115,** 166602 (2015).

[35] Pranab Kumar Das, D. Di Sante, I. Vobornik, J. Fujii, T. Okuda, E. Bruyer, A. Gyenis, B. E. Feldman, J. Tao, R. Ciancio, G. Rossi, M. N. Ali, S. Picozzi, A. Yadzani, G. Panaccione, and R. J. Cava, Nat. Commun. **7,** 10847 (2016).

[36] L. M. Schoop, M. N. Ali, C. Straβer, V. Duppel, S. S. P. Parkin, B. V. Lotsch, and C. R. Ast, Nat. Commun. **7,** 11696 (2016).

[37] R. Lou, J.-Z. Ma, Q.-N. Xu, B.-B. Fu, L.-Y. Kong, Y.-G. Shi, P. Richard, H.-M. Weng, Z. Fang, S.-S. Sun, Q. Wang, H.-C. Lei, T. Qian, H. Ding, and S.-C. Wang, Phys. Rev. B **93,** 241104(R) (2016).

[38] Y. Wu, L.-L. Wang, E. Mun, D. D. Johnson, D. Mou, L. Huang, Y. Lee, S. L. Budko, P. C. Canfield, and A. Kaminski, Nat. Phys. **12,** 667, (2016).

[39] See Supplemental Material at http://link.aps.org/supplemental/10.1103/PhysRevLett.117.127204, which includes Shubnikov-de Haas results and photon energy dependence ARPES data.

[40] Y. L. Wang, L. R. Thoutam, Z. L. Xiao, J. Hu, S. Das, Z. Q. Mao, J. Wei, R. Divan, A. Luican-Mayer, G. W. Crabtree, and W. K. Kwok, Phys. Rev. B **92,** 180402 (2015).

[41] A. B. Pippard, *Magnetoresistance in Metals* (Cambridge University Press, Cambridge, 1989).

[42] P.-J. Guo, H.-C. Yang, B.-J. Zhang, K. Liu, and Z.-Y. Lu, Phys. Rev. B **93,** 235142 (2016).

[43] H. Kitazawa, T. Suzuki, M. Sera, I. Oguro, A. Yanase, A. Hasegawa, and T. Kasuya, J. Magn. Magn. Mater. **31–34,** 421 (1983).

[44] A. Hasegawa, J. Phys. Soc. Jpn. **54,** 677 (1985).

[45] M. G. Zeng, C. Fang, G. Q. Chang, Y.-A. Chen, T. Hsieh, A. Bansil, H. Lin, and L. Fu, arXiv:1504.03492.

[46] A. D. Becke and E. R. Johnson, J. Chem. Phys. **124,** 221101 (2006).

[47] F. Tran and P. Blaha, Phys. Rev. Lett. **102,** 226401 (2009).

[48] P. Zhang, P. Richard, T. Qian, Y.-M. Xu, X. Dai, and H. Ding, Rev. Sci. Instrum. **82,** 043712 (2011).

[49] A. Collaudin, B. Fauqué, Y. Fuseya, W. Kang, and K. Behnia, Phys. Rev. X **5,** 021022 (2015).

[50] H. Weng, C. Fang, Z. Fang, B. A. Bernevig, and X. Dai, Phys. Rev. X **5,** 011029 (2015).

[51] A. Kokalj, Comput. Mater. Sci. **28,** 155 (2003).